Electronic Supplementary Material (ESI) for Inorganic Chemistry Frontiers.

Electronic Supporting Information

Dual-ligands-functionalized dodeca-nuclear-lanthanide-tungsten-cluster incorporated selenotungstates and fluorescence detection of dipicolonic acid (an anthrax biomarker)

Tiantian Gong, Sen Yang, Zixu Wang, Mengyao Li, Siyu Zhang, Jiancai Liu,* Lijuan Chen,* Junwei Zhao*

Henan Key Laboratory of Polyoxometalate Chemistry, College of Chemistry and Chemical Engineering, Henan University, Kaifeng 475004, China

Scheme S1 Chemical structures and acronyms of 2,3-pyrazine dicarboxylic acid (a), fumaric acid (b), tris(hydroxymethyl) aminomethane (c), ethylendiamine (d), 1.3,5-benzenreicarboxylic acid (e), isonicotinic acid (f) and 2,5-pypyridine-dicarboxylic acid (g).

Scheme S2 Chemical structures of DPA (a), 2,3-pyridine dicarboxylic acid (b), 2,5-pyridine dicarboxylic acid (c), 2-picolinic acid (d), nicotinic acid (e), benzoic acid (f), p-phthalic acid (g), m-phthalic acid (h); amino acids:(glycine (i), glutathione (j).

Fig. S1 (a–d) Experimental and simulative PXRD patterns of **1**–**4**.

Fig. S2 (a–d) IR spectra and the corresponding crystal colors of **1**–**4**.

Fig. S3 (a–d) TG curves of **1**–**4**.

Fig. S4 The highlighted O2 atom in the center of symmetry of the **4a** polyanion.

Fig. S5 View of a "hourglass-shaped" $\{W_6(HFMA)_2\}$ cluster.

Fig. S6 View of the seven-membered formed by the $Eu1^{3+}$ ion and five-membered ring formed by the $Eu2^{3+}$ ion.

Fig. S7 (a, b) Coordination geometries of $Eu1^{3+}$ and $Eu2^{3+}$ ions.

Fig. S8 Views of $\{Eu_4W_8\}$ cluster in three different orientations: (a) front view, (b) rotated view, (c) bottom view.

Fig. S9 (a) "N"-shaped $\{W_6\}$ segment. (b, c) Pseudo-hexagonal configuration of the $\{Eu_4W_2\}$ segment.

Fig. S10 The edge lengths (a) and two adjacent angles (b) of parallelogram $\{Eu_4\}$ cluster.

Fig. S11 (a) View of the parallelogram built by $\{Eu_4\}$ cluster. (b) The angle between the parallelogram and the triangle (Eu1, Eu2, W1).

Fig. S12 (a) View of Layer A in **4a** along the *c* axis. (b) View of Layer B in **4a** along the *c* axis. (c) The 3-D stacking mode of **4a** along the *b* axis. (d) The repeating unit of **4a**.

Fig. S13. The CIE 1931 chromaticity diagram of solid-state **4**.

Fig. S14 (a) The ESI-MS spectrum of **4** in aqueous solution. (b) The UV-visible spectra of **4** in aqueous solution in 48 h.

Fig. S15 The ratio of $I_{5D0}\rightarrow I_{7F2}$ / $I_{5D0}\rightarrow I_{7F1}$ with different DPA concentrations.

Fig. S16 Evolution of the intensity ratio (I/I_0) with various concentrations of DPA in three trials.

Fig. S17 The emission spectral evolution of **4** with different concentrations (0–325 μM) of different detection substances: (a) DPA; (b) 2,3-PDCA; (c) 2,5-PDCA; (d) 2-PA; (e) NA; (f) BA ;(g) *p*-PA; (h) *m*-PA; (i) H_3BTC; (j) Gly; (k) GSH; (l) K^+; (m) Mg^{2+}; (n) Ca^{2+}; (o) Cl^-; (p) CH_3COO^-.

Fig. S18 (a) FL emission spectra of **4** in the presence of DPA and the interferents (325 μM). (b) Variation of the FL emission intensity of $^5D_0\rightarrow{}^7F_2$ transition of **4** with different interferents. (c) Variation of the FL emission intensity of $^5D_0\rightarrow{}^7F_2$ transition of **4** in the simultaneous presence of DPA and interferents (325 μM) (In the order: (1) DPA, (2) 2,3-PDCA, (3) 2,5-PDCA, (4) 2-PA, (5) NA, (6) BA, (7) p-PA, (8) m-PA, (9) H_3BTC, (10) Gly, (11) GSH, (12) K^+, (13) Mg^{2+}, (14) Ca^{2+}, (15) Cl^-, (16) CH_3COO^-).

Fig. S19 The lifetime decay curves of **4** obtained by monitoring the emission at 613 nm and the excitation at 395 nm in the presence of each interferent with different concentrations (0 to 300 μM): (a) 2-PA, (b) Gly, (c) Mg^{2+} (Inset: the variation of average lifetime of **4** with the concentration of each interferent).

Fig. S20 (a) FL lifetime decay curves of **4** in H_2O with different DPA concentrations. (b) Variation of the average lifetime of **4** in H_2O with different DPA concentrations.

Fig. S21 FL lifetime decay curves of **4** in the D_2O system with different DPA concentrations (0 μM (a), 100 μM (b), 200 μM (c), 300 μM(d)).

Fig. S22 (a) FL spectra of $Eu(NO_3)_3{\cdot}6H_2O$ (3 mg / mL) in H_2O with different DPA concentrations (λ_{ex} = 396 nm). (b) Variation of the FL emission intensity at 592 nm of $Eu(NO_3)_3{\cdot}6H_2O$ with the DPA concentration in H_2O.

Fig. S23 (a) FL spectra of $Eu(NO_3)_3{\cdot}6H_2O$ (3 mg / mL) in the D_2O system with different DPA concentrations (λ_{ex} = 396 nm). (b) Variation of the FL emission intensity at 592 nm of $Eu(NO_3)_3{\cdot}6H_2O$ (3 mg / mL) with the DPA concentration in the D_2O system. (c) FL lifetime decay curves of $Eu(NO_3)_3{\cdot}6H_2O$ (3 mg / mL) in H_2O with different DPA concentrations (inset: the change of the lifetime of $Eu(NO_3)_3{\cdot}6H_2O$ (3 mg / mL) at 592 nm with DPA concentration) (λ_{em} = 592 nm). (d) FL lifetime decay curves of Eu^{3+} in D_2O with different DPA concentrations (inset: the change of the lifetime of $Eu(NO_3)_3{\cdot}6H_2O$ (3 mg / mL) at 592 nm with the DPA concentration) (λ_{em} = 592 nm).

Table S1. Crystallographic data and structure refinements for **1**–**4**.

Table S2. The ratios of $I(^5D_0\rightarrow{}^7F_2)$ / $I(^5D_0\rightarrow{}^7F_1)$ for **4** in aqueous solution with different DPA concentrations.

Table S3. The standard deviations for the **4**-based FL sensor.

Table S4. Performance comparison of several sensors for the detection of DPA.

Table S5. Detection results of DPA in tap water and human serum sample.

Table S6. Summary of the lifetimes of Eu^{3+} in H_2O and D_2O with different DPA concentrations and the calculated q values.

Materials and measurements

All chemicals and reagents were purchased commercially and used without further purification. IR spectra were recorded on a Perkin–Elmer FT–IR spectrophotometer by using KBr pellets in the wavenumber range of 4000–450 cm^{-1}. Elemental analyses (N, H, C) were performed on a Perkin–Elmer 2400–II CHNS analyzer. Inductively coupled plasma-atomic emission spectroscopy (ICP−AES) analyses were conducted on a Perkin–Elmer Optima 2000 ICP−AES spectrometer. Powder X−ray diffraction (PXRD) patterns were measured on a Bruker AXS D8 Advance diffractometer with Cu *K*α radiation (*λ* = 1.54056 Å) at 293 K. Thermogravimetric (TG) analyses were carried out on a Bruker Tensor–II TGA instrument under a flowing N_2 atmosphere (temperature range: 25–1000 °C, heating rate: 10 °C min^{-1}). Electrospray ionization mass spectrometry (ESI–MS) was performed on an AB SCIEX Triple TOF 4600 spectrometer operating in negative ion mode and the data was analyzed using the Peakview 2.0 software provided. Photoluminescence spectra (excitation spectra, emission spectra and lifetimes) were collected by Edinburgh FLS 980 Analytical Instrument apparatus equipped with a 450 W xenon lamp and a μF900H high-energy microsecond flashlamp as the excitation sources.

X-ray crystallography

A good-quality single-crystal of **1** was picked carefully and its diffraction data were collected on a Bruker D8 Venture Photon II diffractometer equipped with CCD two-dimensional detector using monochromated Mo Kα radiation (λ = 0.71073 Å) at 296 K. Routine Lorentz and polarization corrections were applied and a multi-scan absorption correction was utilized with the SADABS program. Direct methods were used to solve the structure, refined on F^2 by full-matrix least-squares method using the SHELXTL–97 program.[1-3] All H atoms connected to N and C atoms were generated geometrically and refined isotropically as a riding model using the default SHELXTL parameters. No hydrogen atoms associated with water molecules are located from the difference Fourier map. All nonhydrogen atoms are refined anisotropically except for some sodium, carbon, oxygen atoms and water molecules. In the refinement of **4**, twelve $[H_2N(CH_3)_2]^+$ cations, two Cs^+ cations, two Na^+ cations and twenty one lattice water molecules in the molecular unit were found from the Fourier maps. However, there are still solvent accessible voids in the check cif report of crystal structure of **4**, indicating that some cations or lattice water molecules should exist in the structure that can't be found from the weak residual electron peaks. Therefore, on the basis of charge balance, elemental analysis and TG analysis, two $[H_2N(CH_3)_2]^+$ cations and nine lattice water molecules were directly added to the molecular formula of **4**. The crystallographic data and structure refinements for **1**–**4** are demonstrated in Table S1. Crystallographic data and structure refinements for **1**–**4** reported in this paper have been deposited in the Cambridge Crystallographic Data Centre with CCDC 2244122-2244125 for **1**–**4**. These data can be obtained free of charge from the Cambridge Crystallographic Data Centre via www.ccdc.cam.ac.uk/data_request/cif.

Synthesis of $[H_2N(CH_3)_2]_{16}Na_2[Ce_4(H_2O)_6(HPZDA)_2(HFMA)_2W_8O_{21}][B\text{-}\alpha\text{-}SeW_9O_{33}]_4\cdot 29H_2O$ (1). $Na_2WO_4\cdot 2H_2O$ (5.002 g, 15.165 mol), Na_2SeO_3 (0.101 g, 0.584 mmol), dimethylamine hydrochloride (1.502 g, 18.419 mmol), 2,3-pyrazinedicarboxylic acid (H_2PZDA) (0.401 g, 2.385 mmol) and glacial acetic acid (CH_3COOH) (2.0 mL, 34.972 mmol) were dissolved in 28 mL distilled water under stirring, and the pH value of the solution was adjusted to

3.00 by 6 M HCl. Then, $Ce(NO_3)_3·6H_2O$ (0.501 g, 1.154 mmol) and fumaric acid (H_2FMA) (0.202 g, 1.740 mmol) were consecutively added to the solution and the final pH value of the solution was kept at 3.00 by 2 M NaOH. This solution was stirred for 20 min, heated at 60 °C for 2 h, cooled to room temperature and filtered. About several weeks later, yellow block crystals were obtained through the evaporation process. Yield: 0.501 g (25.85 % based on Na_2SeO_3). Anal. calcd. (found%) for $C_{52}H_{210}Ce_4N_{20}Na_2O_{204}Se_4W_{44}$ (**1**): C 4.66 (4.70), H 1.58 (1.73), N 2.09 (2.18), W 60.40 (60.22), Se 2.36 (2.20), Ce 4.19 (4.15), Na 0.34 (0.25).

Synthesis of $[H_2N(CH_3)_2]_{16}Na_2[Pr_4(H_2O)_6(HPZDA)_2(HFMA)_2W_8O_{21}][B\text{-}\alpha\text{-}SeW_9O_{33}]_4·29H_2O$ (2). The synthetic procedure of **2** was similar to **1** except that $Ce(NO_3)_3·6H_2O$ was replaced by $Pr(NO_3)_3·6H_2O$ (0.502 g, 1.154 mmol). Green block crystals of **2** were obtained. Yield: 0.490 g (25.28 % based on Na_2SeO_3). Anal. calcd. (found%) for $C_{52}H_{210}Pr_4N_{20}Na_2O_{204}Se_4W_{44}$ (**2**): C 4.66 (4.52), H 1.58 (1.75), N 2.09 (2.05), W 60.39 (60.12), Se 2.36 (2.15), Pr 4.21 (3.99), Na 0.34 (0.32).

Synthesis of $[H_2N(CH_3)_2]_{16}Na_2[Nd_4(H_2O)_6(HPZDA)_2(HFMA)_2W_8O_{21}][B\text{-}\alpha\text{-}SeW_9O_{33}]_4·29H_2O$ (3). The synthetic procedure of **3** was similar to **1** except that $Ce(NO_3)_3·6H_2O$ was replaced by $Nd(NO_3)_3·6H_2O$ (0.499 g, 1.138 mmol). Purple block crystals of **3** were obtained. Yield: 0.475 g (24.47 % based on Na_2SeO_3). Anal. calcd. (found%) for $C_{52}H_{210}Nd_4N_{20}Na_4O_{204}Se_4W_{44}$ (**3**): C 4.66 (4.57), H 1.58 (1.77), N 2.09 (2.12), W 60.33 (60.55), Se 2.36 (2.25), Nd 4.30 (4.44), Na 0.34 (0.30).

Synthesis of $[H_2N(CH_3)_2]_{14}Cs_2Na_2[Eu_4(H_2O)_6(HPZDA)_2(HFMA)_2W_8O_{21}][B\text{-}\alpha\text{-}SeW_9O_{33}]_4·30H_2O$ (4). The synthetic procedure of **4** was similar to **1** except that $Ce(NO_3)_3·6H_2O$ was replaced by $Eu(NO_3)_3·6H_2O$ (0.500 g, 1.121 mmol), and add CsCl (0.300 g, 1.782 mmol). Colorless block crystals of **4** were obtained. Yield: 0.200 g (10.28 % based on Na_2SeO_3). Anal. calcd. (found%) for $C_{48}H_{196}Cs_2Eu_4N_{16}Na_2O_{205}Se_4W_{44}$ (**4**): C 4.24 (4.42), H 1.45 (1.61), Cs 1.95 (2.16), N 1.65 (1.85), W 59.47 (59.69), Se 2.32 (2.15), Eu 4.47 (4.35), Na 0.34 (0.38).

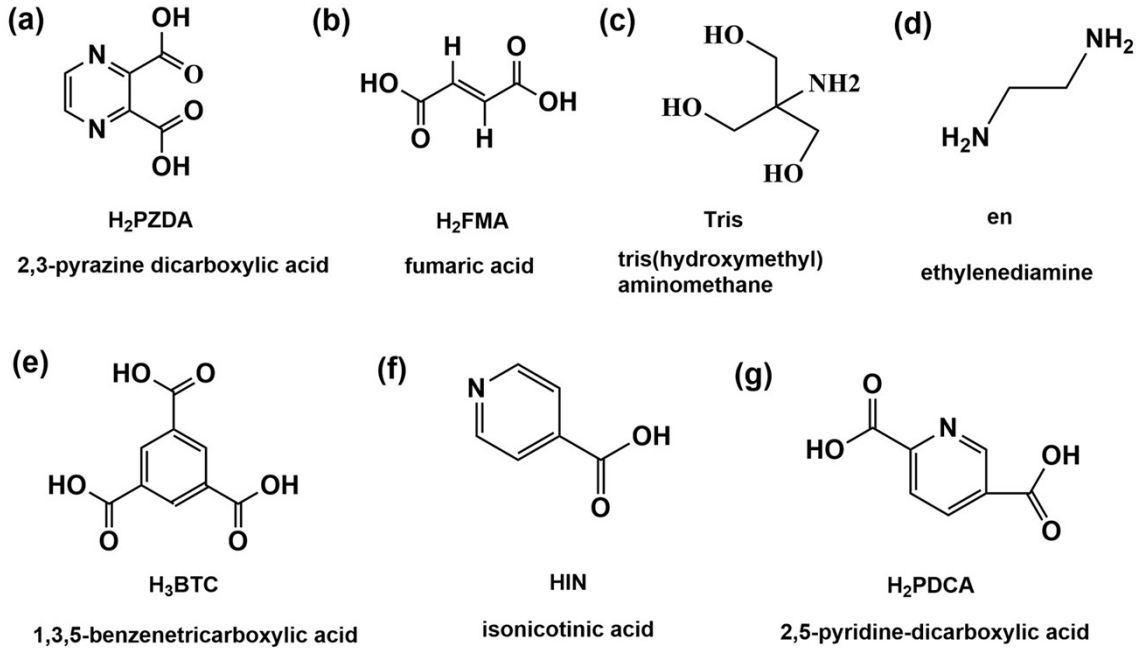

Scheme S1 Chemical structures and acronyms of 2,3-pyrazine dicarboxylic acid (a), fumaric acid (b), tris(hydroxymethyl) aminomethane (c), ethylendiamine (d), 1.3,5-benzenreicarboxylic acid (e), isonicotinic acid (f) and 2,5-pypyridine-dicarboxylic acid (g).

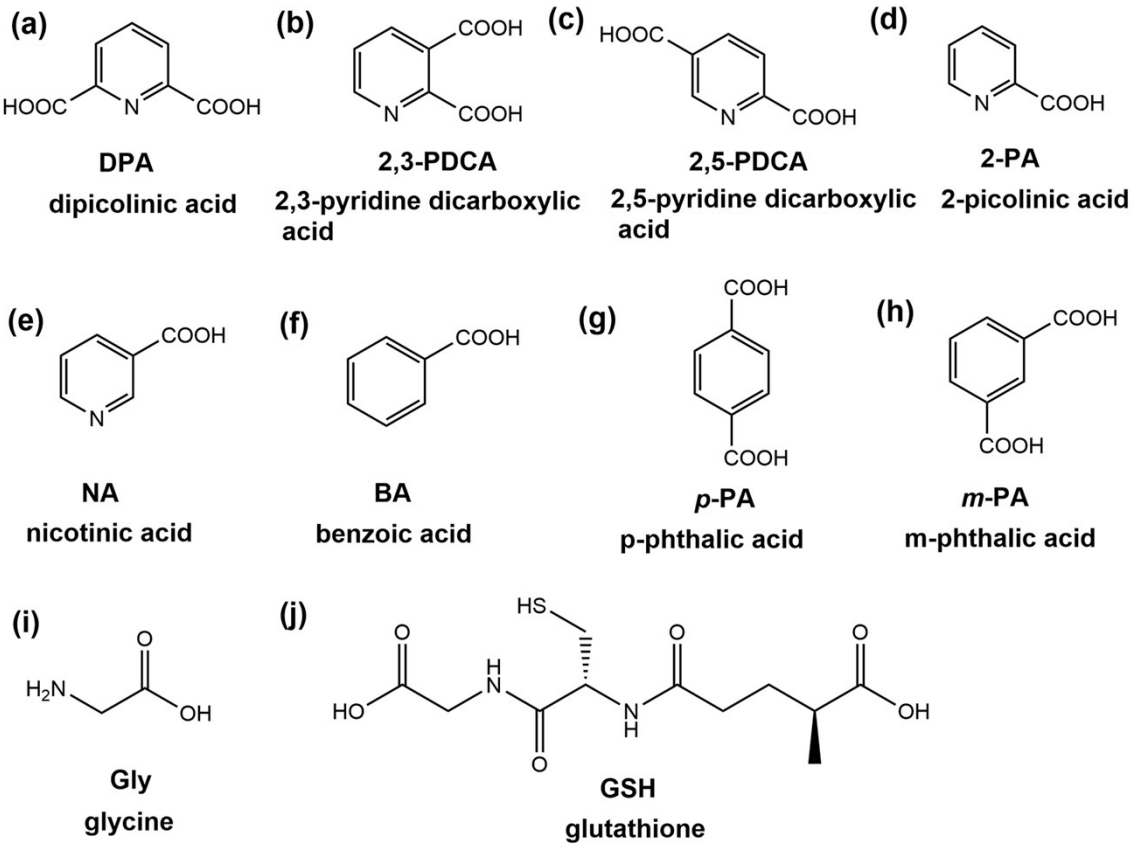

Scheme S2 Chemical structures of DPA (a), 2,3-pyridine dicarboxylic acid (b), 2,5-pyridine dicarboxylic acid (c), 2-picolinic acid (d), nicotinic acid (e), benzoic acid (f), p-phthalic acid (g), m-phthalic acid (h); amino acids:(glycine (i), glutathione (j).

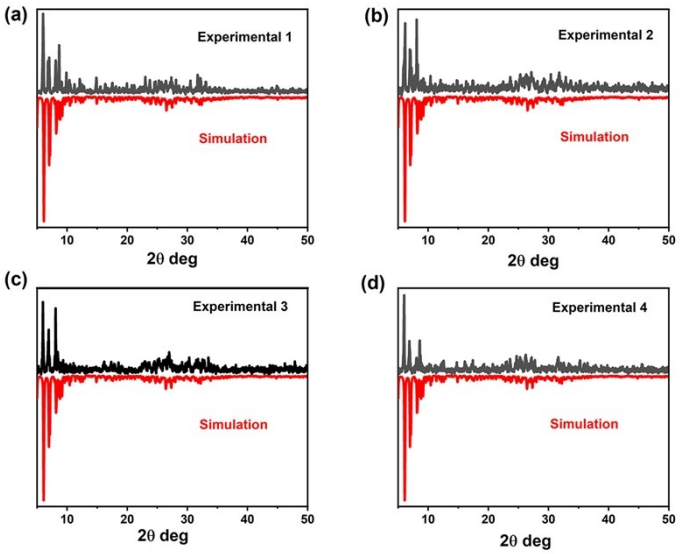

Fig. S1 (a–d) Experimental and simulative PXRD patterns of **1**–**4**.

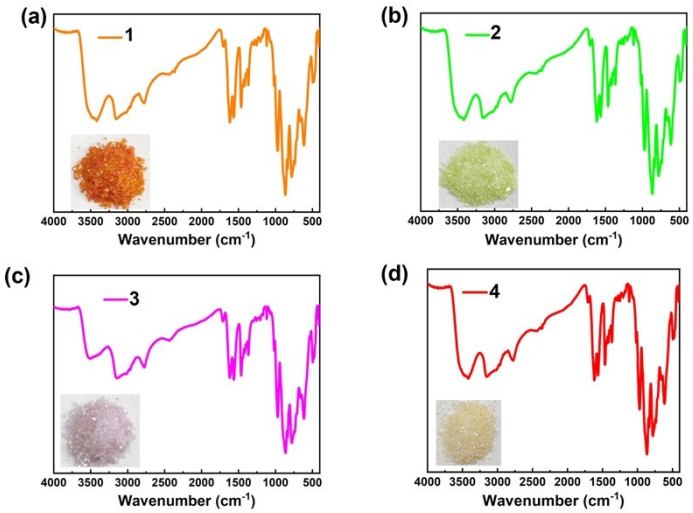

Fig. S2 (a–d) IR spectra and the corresponding crystal colors of **1**–**4**.

IR spectra of **1**–**4** were recorded by a Perkin–Elmer FT–IR spectrophotometer (Fig. S2). Basically, it can be observed that four compounds have similar characteristic peaks, which indicates that they have the same anionic framework structure. Four characteristic vibrations ν(W–O_t), ν(Se–O_a), ν(W–O_b), and ν(W–O_c) are observed at 971, 866, 835, 780, 739 cm^{-1} for **1**, 969, 866, 833, 780, 739 cm^{-1} for **2**, 970, 864, 778, 739 cm^{-1} for **3**, 970, 866, 833, 781, 740 cm^{-1} for **4**, severally.[4] In addition, the absorption bands at 1638–1021 cm^{-1} can be regarded as characteristic peaks of $HPZDA^-$ and $HFMA^-$ ligands. Wherein, the asymmetric and symmetric stretching vibrations of carboxylic groups appear at 1626–1576 cm^{-1} and 1464–1366 cm^{-1}, respectively.[5] Besides, three bands ν(N–H) (3153 cm^{-1}), ν(C–H) (2780 cm^{-1}) and ν(C–N) (1463 cm^{-1}) for **1**, ν(N–H) (3157 cm^{-1}), ν(C–H) (2782 cm^{-1}) and ν(C–N) (1465 cm^{-1}) for **2**, ν(N–H) (3148 cm^{-1}), ν(C–H) (2782 cm^{-1}) and ν(C–N) (1462 cm^{-1}) for **3**, ν(N–H) (3151 cm^{-1}), ν(C–H) (2777 cm^{-1}) and ν(C–N) (1462 cm^{-1}) for **4** that demonstrate the existence of dimethylamine groups in the structures.[4] In the high-wavenumber region, the broad absorption bands at around 3410 cm^{-1} and 1615 cm^{-1} are typical features of lattice and coordinate water molecules.

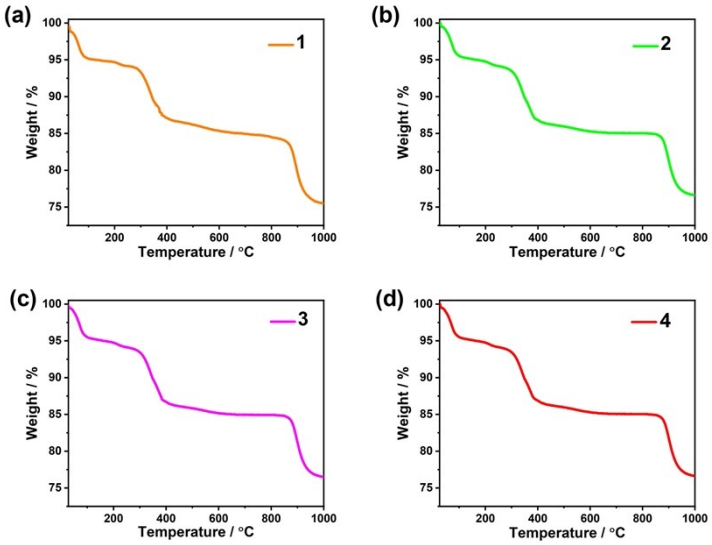

Fig. S3 (a–d) TG curves of **1**–**4**.

The thermal stability measurements of **1**–**4** were performed under N_2 atmosphere with a heating speed of 10 °C /min from 25 to 1000 °C. The TG curves of **1**–**4** display similar three-step weight loss. The first weight loss of 4.90 % (calcd. 4.71 %) for **1**, 4.95 % (calcd. 4.71 %) for **2**, 5.01 % (calcd. 4.70 %) for **3** and 4.95 % (calcd. 4.62 %) for **4** from 25 to 200 °C belongs to the liberation of 29 lattice water molecules and 6 coordination water molecules for **1**–**3**, 30 lattice water molecules and 6 coordination water molecules for **4**. Keeping heating to 750 °C, the second weight loss of 10.20 % (calcd. 10.43 %) for **1**, 10.15 % (calcd. 10.41 %) for **2**, 10.19 % (calcd. 10.42 %) for **3** and 9.80 % (calcd. 9.45 %) for **4** occurs, which corresponds to the loss of 16 dimethylamine molecules, 2 H_2PDCA ligands, 2 H_2FMA ligands and dehydration of 12 protons for **1**–**3**, and 14 dimethylamine molecules, 2 H_2PDCA ligands, 2 H_2FMA ligands and dehydration of 10 protons for **4**. Finally, as the temperature continues to rise, the main polyoxoanion skeletons of **1**–**4** begin to decompose.

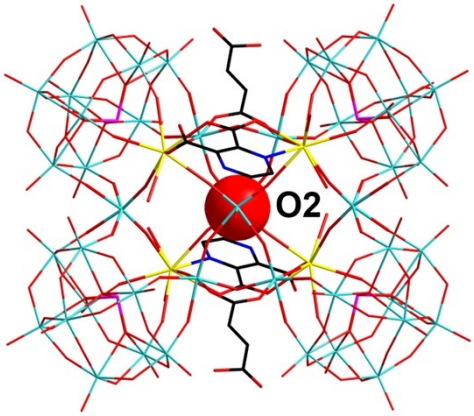

Fig. S4 The highlighted O2 atom in the center of symmetry of the **4a** polyanion.

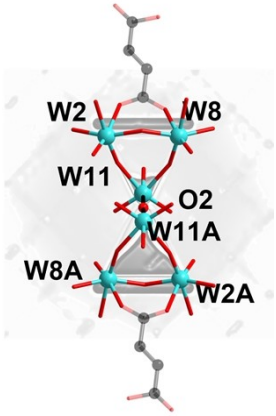

Fig. S5 View of a "hourglass-shaped" $\{W_6(HFMA)_2\}$ cluster.

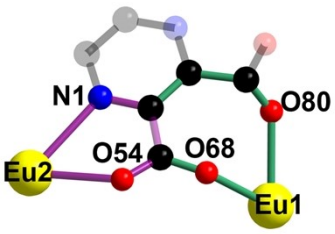

Fig. S6 View of the seven-membered formed by the $Eu1^{3+}$ ion and five-membered ring formed by the $Eu2^{3+}$ ion.

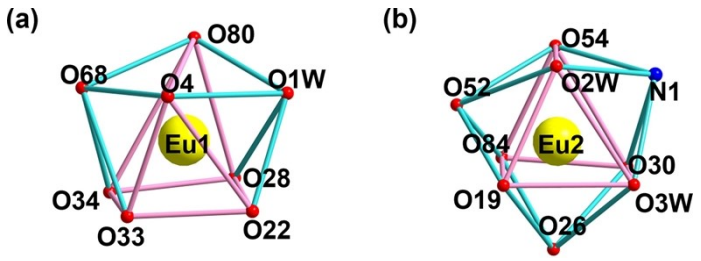

Fig. S7 (a, b) Coordination geometries of $Eu1^{3+}$ and $Eu2^{3+}$ ions.

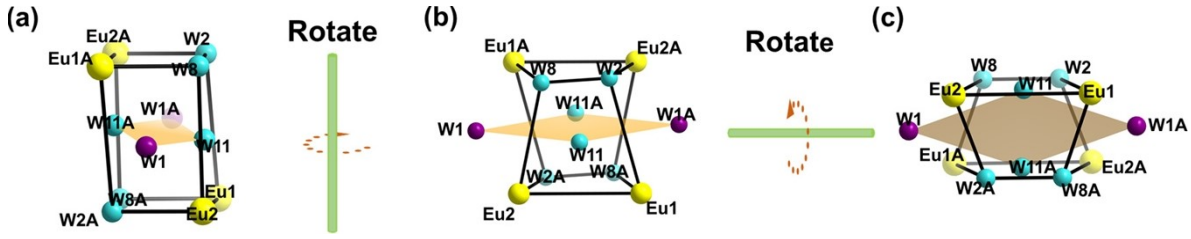

Fig. S8 Views of $\{Eu_4W_8\}$ cluster in three different orientations: (a) front view, (b) rotated view, (c) bottom view.

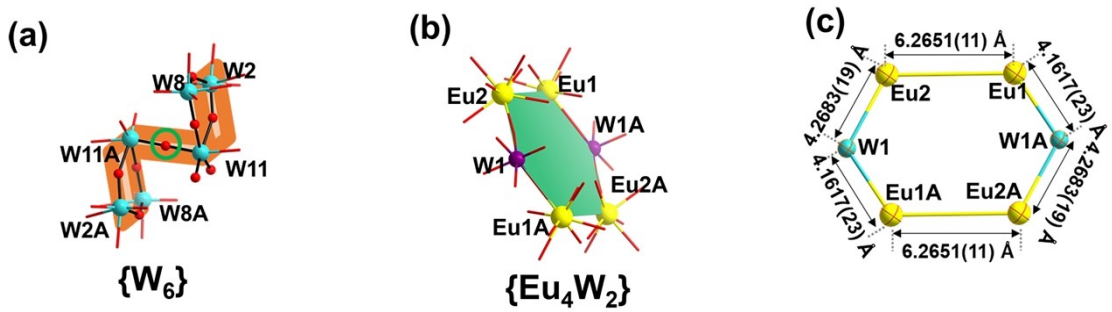

Fig. S9 (a) "N"-shaped $\{W_6\}$ segment. (b, c) Pseudo-hexagonal configuration of the $\{Eu_4W_2\}$ segment.

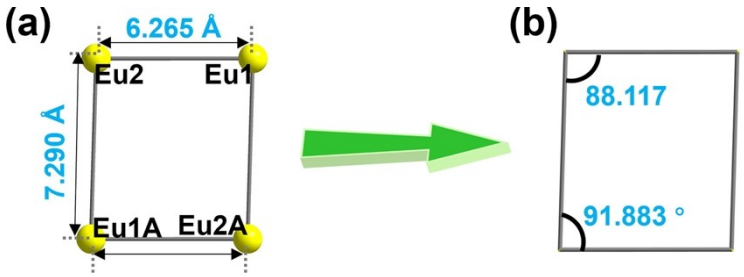

Fig. S10 The edge lengths (a) and two adjacent angles (b) of parallelogram $\{Eu_4\}$ cluster.

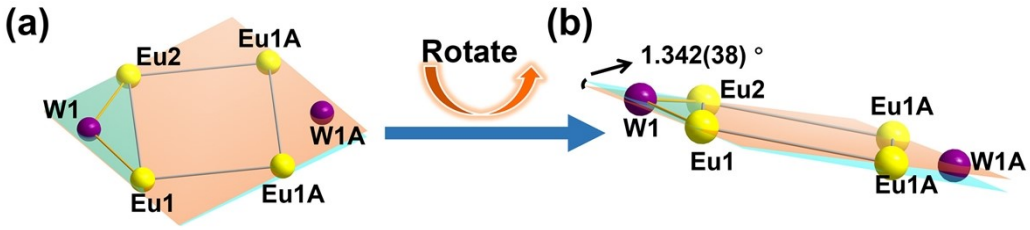

Fig. S11 (a) View of the parallelogram built by $\{Eu_4\}$ cluster. (b) The angle between the parallelogram and the triangle (Eu1, Eu2, W1).

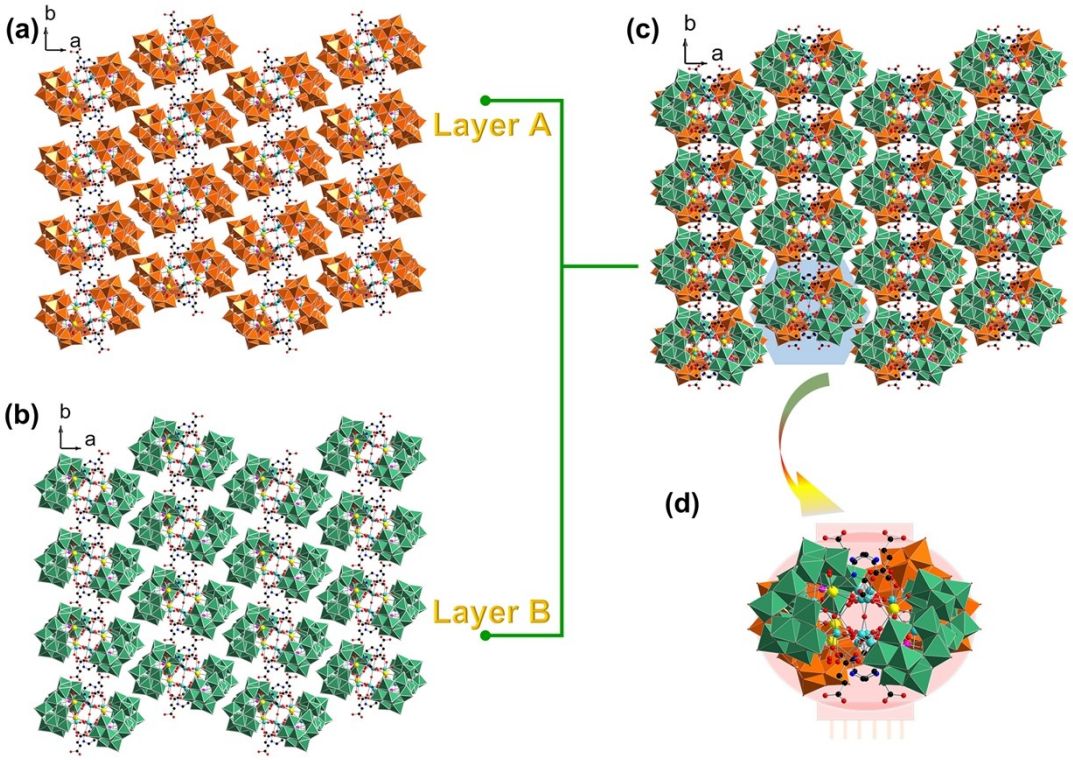

Fig. S12 (a) View of Layer A in **4a** along the *c* axis. (b) View of Layer B in **4a** along the *c* axis. (c) The 3-D stacking mode of **4a** along the *b* axis. (d) The repeating unit of **4a**.

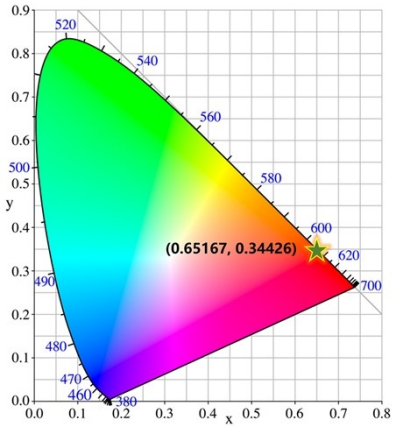

Fig. S13 The CIE 1931 chromaticity diagram of solid-state **4**.

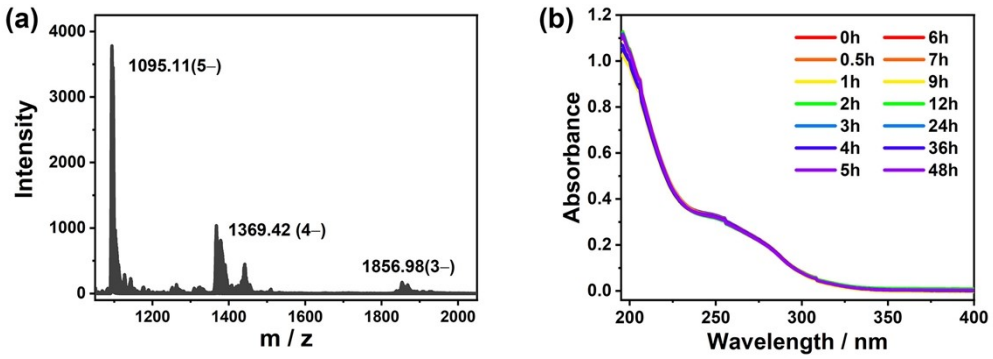

Fig. S14 (a) The ESI-MS spectrum of **4** in aqueous solution. (b) The UV-visible spectra of **4** in aqueous solution in 48 h.

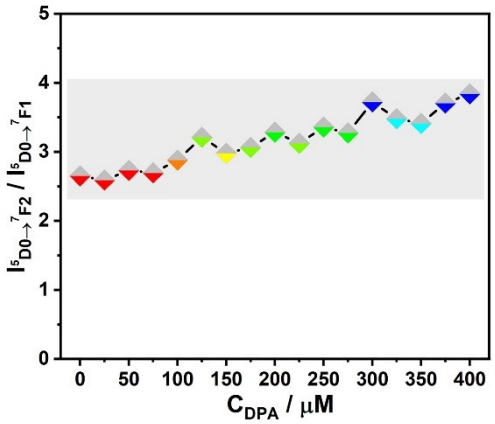

Fig. S15 The ratio of $I_{5D0}\rightarrow I_{7F2}$ / $I_{5D0}\rightarrow I_{7F1}$ with different DPA concentrations.

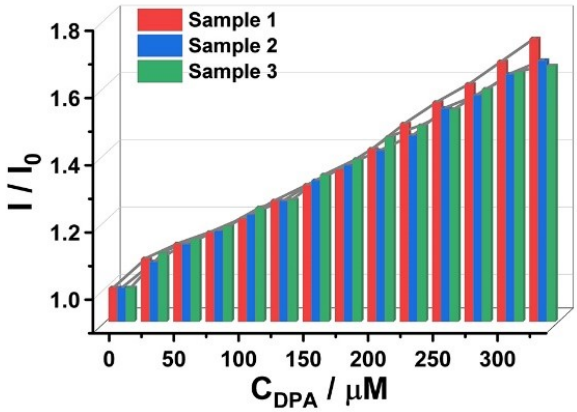

Fig. S16 Evolution of the intensity ratio (I/I_0) with various concentrations of DPA in three trials.

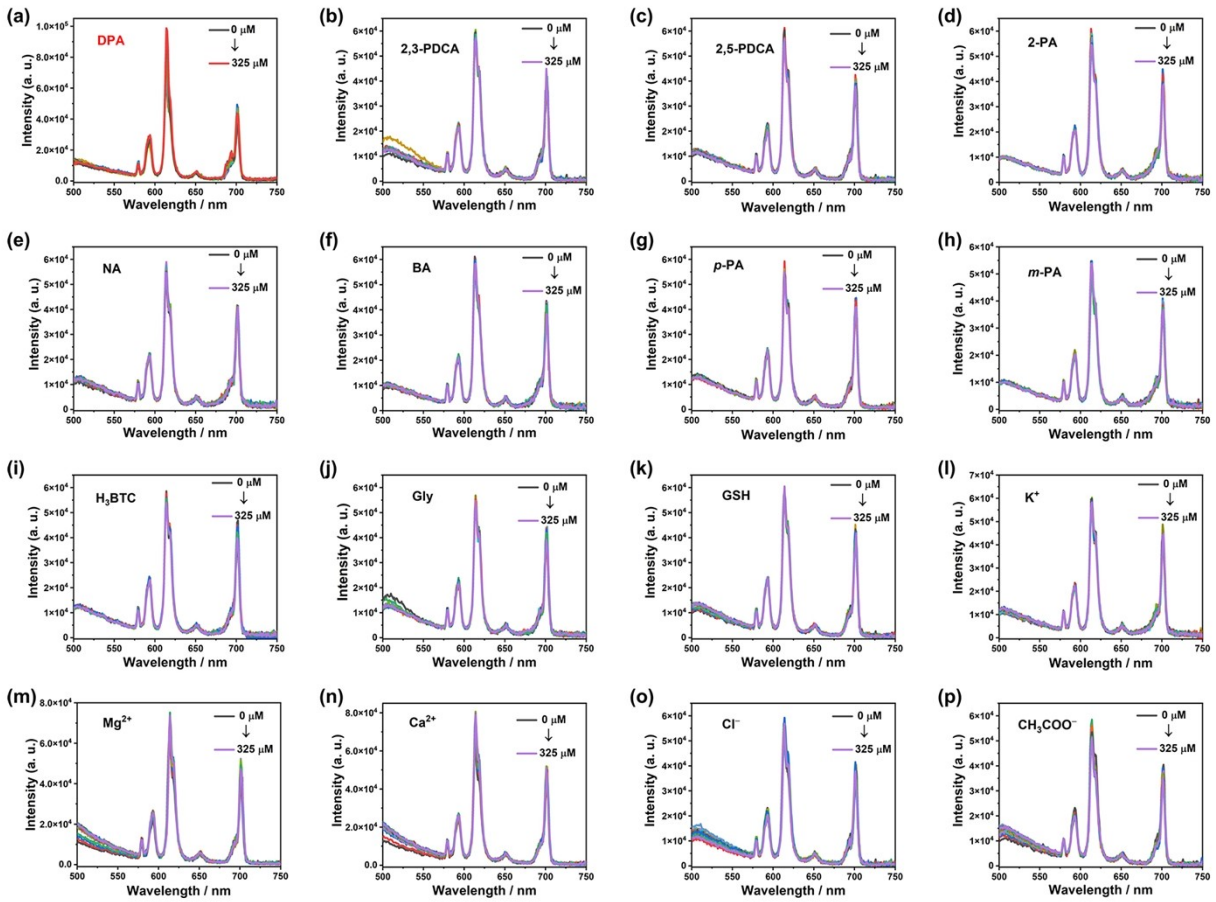

Fig. S17 The emission spectral evolution of **4** with different concentrations (0–325 μM) of different detection substances: (a) DPA; (b) 2,3-PDCA; (c) 2,5-PDCA; (d) 2-PA; (e) NA; (f) BA ;(g) *p*-PA; (h) *m*-PA; (i) H_3BTC; (j) Gly; (k) GSH; (l) K^+; (m) Mg^{2+}; (n) Ca^{2+}; (o) Cl^-; (p) CH_3COO^-.

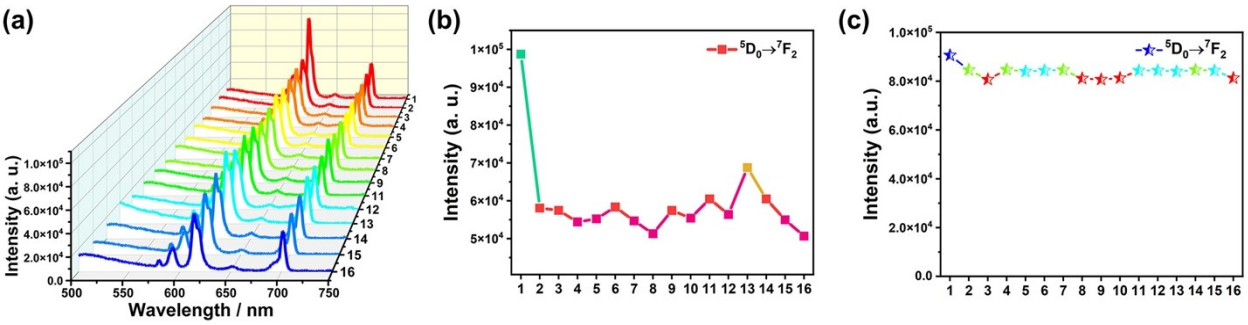

Fig. S18 (a) FL emission spectra of **4** in the presence of DPA and the interferents (325 μM). (b) Variation of the FL emission intensity of $^5D_0 \rightarrow {}^7F_2$ transition of **4** with different interferents. (c) Variation of the FL emission intensity of $^5D_0 \rightarrow {}^7F_2$ transition of **4** in the simultaneous presence of DPA and interferents (325 μM) (In the order: (1) DPA, (2) 2,3-PDCA, (3) 2,5-PDCA, (4) 2-PA, (5) NA, (6) BA, (7) p-PA, (8) m-PA, (9) H_3BTC, (10) Gly, (11) GSH, (12) K^+, (13) Mg^{2+}, (14) Ca^{2+}, (15) Cl^-, (16) CH_3COO^-).

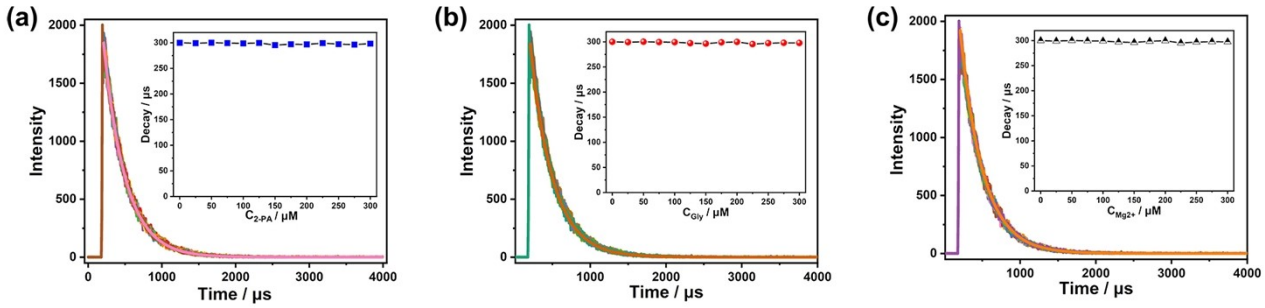

Fig. S19 The lifetime decay curves of **4** obtained by monitoring the emission at 613 nm and the excitation at 395 nm in the presence of each interferent with different concentrations (0 to 300 μM): (a) 2-PA, (b) Gly, (c) Mg^{2+} (Inset: the variation of average lifetime of **4** with the concentration of each interferent).

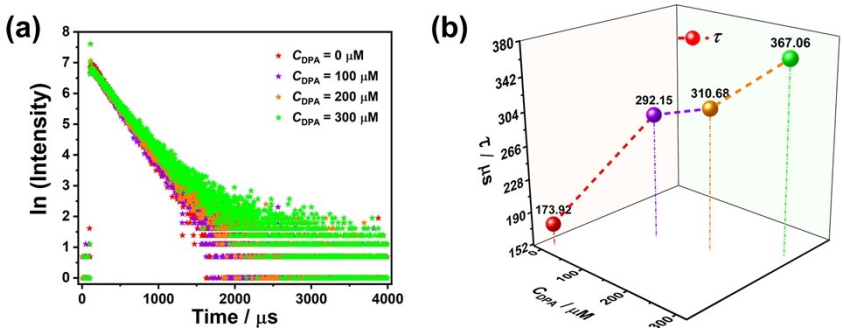

Fig. S20 (a) FL lifetime decay curves of **4** in H_2O with different DPA concentrations. (b) Variation of the average lifetime of **4** in H_2O with different DPA concentrations.

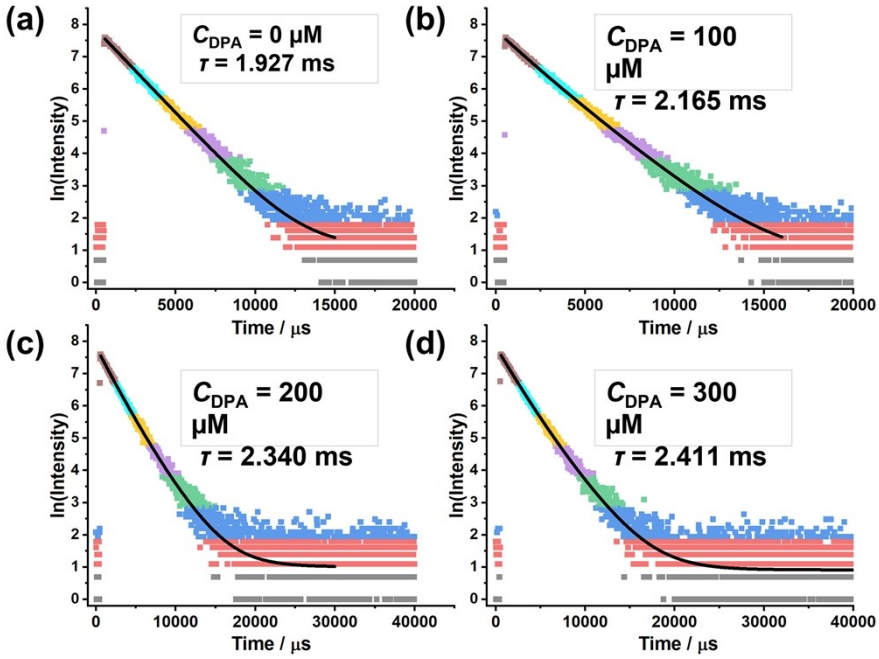

Fig. S21 FL lifetime decay curves of **4** in the D_2O system with different DPA concentrations (0 μM (a), 100 μM (b), 200 μM (c), 300 μM(d)).

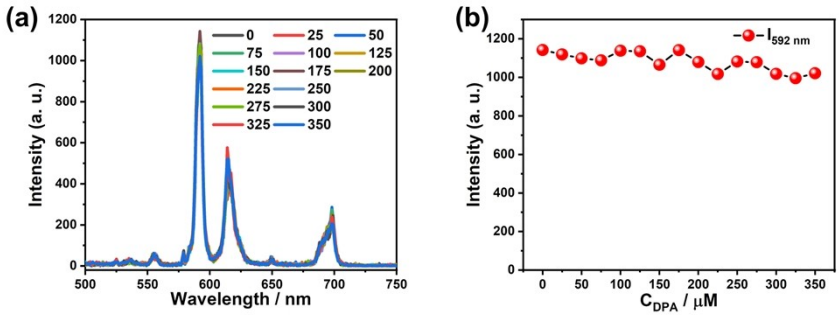

Fig. S22 (a) FL spectra of $Eu(NO_3)_3{\cdot}6H_2O$ (3 mg / mL) in H_2O with different DPA concentrations (λ_{ex} = 396 nm). (b) Variation of the FL emission intensity at 592 nm of $Eu(NO_3)_3{\cdot}6H_2O$ with the DPA concentration in H_2O.

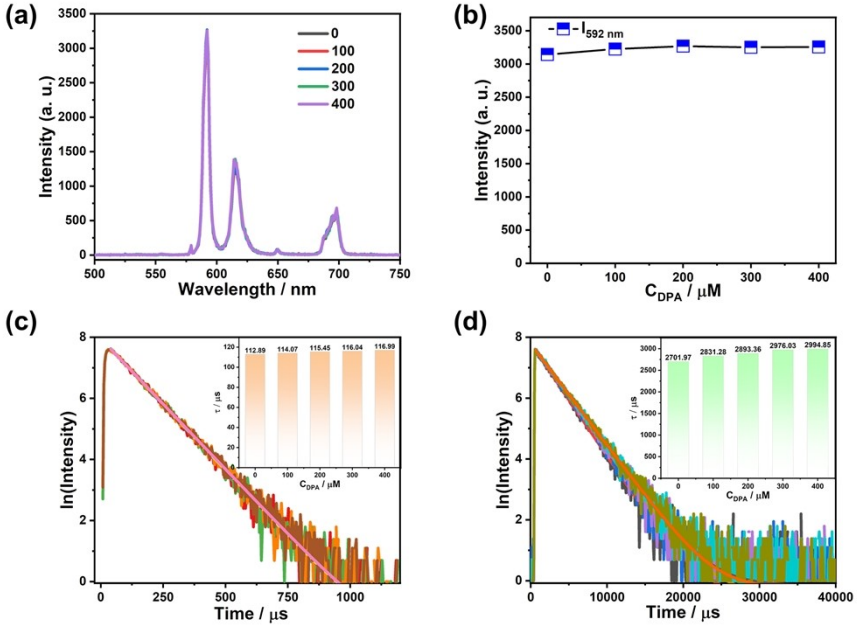

Fig. S23 (a) FL spectra of $Eu(NO_3)_3{\cdot}6H_2O$ (3 mg / mL) in the D_2O system with different DPA concentrations (λ_{ex} = 396 nm). (b) Variation of the FL emission intensity at 592 nm of $Eu(NO_3)_3{\cdot}6H_2O$ (3 mg / mL) with the DPA concentration in the D_2O system. (c) FL lifetime decay curves of $Eu(NO_3)_3{\cdot}6H_2O$ (3 mg / mL) in H_2O with different DPA concentrations (inset: the change of the lifetime of $Eu(NO_3)_3{\cdot}6H_2O$ (3 mg / mL) at 592 nm with DPA concentration) (λ_{em} = 592 nm). (d) FL lifetime decay curves of Eu^{3+} in D_2O with different DPA concentrations (inset: the change of the lifetime of $Eu(NO_3)_3{\cdot}6H_2O$ (3 mg / mL) at 592 nm with the DPA concentration) (λ_{em} = 592 nm).

Table S1. Crystallographic data and structure refinements for **1**–**4.**

	1	**2**	**3**	**4**
Empirical formula	$C_{52}H_{210}Ce_4N_{20}Na_2O_{204}Se_4W_{44}$	$C_{52}H_{210}Pr_4N_{20}Na_2O_{204}Se_4W_{44}$	$C_{52}H_{210}Nd_4N_{20}Na_2O_{204}Se_4W_{44}$	$C_{48}H_{196}Cs_2Eu_4N_{16}Na_2O_{205}Se_4W_{44}$
Formula weight	13392.10	13395.26	13408.58	13603.09
Crystal system	Monoclinic	Monoclinic	Monoclinic	Monoclinic
Space group	*C2/c*	*C2/c*	*C2/c*	*C2/c*

a, Å	45.0061(8)	44.9143(7)	44.8905(11)	44.624(2)
b, Å	15.5833(4)	15.5261(3)	15.4986(5)	15.5951(8)
c, Å	40.9321(9)	40.8082(7)	40.7977(11)	40.822(3)
α, deg	90	90	90	90
β, deg	119.1560(10)	119.2310(10)	119.2530(10)	119.1010(10)
γ, deg	90	90	90	90
V, Å^{-3}	25070.1(10)	24833.5(7)	24764.7(12)	24822(3)
Z	4	4	4	4
μ, mm^{-1}	21.495	21.752	21.864	22.275
F(000)	23760	23776	23792	24048
D_c, g cm^{-3}	3.548	3.583	3.596	3.640
T, K	150(2) K	150(2) K	150(2) K	150(2) K
Limiting indices	–53 ≤ *h* ≤ 52, –18 ≤ *k* ≤ 18, –40 ≤ *l* ≤ 40	–53 ≤ *h* ≤ 53, –15 ≤ *k* ≤ 18, –48 ≤ *l* ≤ 42	–53 ≤ *h* ≤ 53 –18 ≤ *k* ≤ 16 -48 ≤ *l* ≤ 42	–53 ≤ *h* ≤ 39, –16 ≤ *k* ≤ 18, –48 ≤ *l* ≤ 48
Reflections collected/unique	71570 / 21643	86830 / 21864	68544 / 21785	86923 / 21987
R_{int}	0.0732	0.0310	0.0493	0.0758
Data/restrains/ parameters	21643 / 90 / 1439	21864 / 0 / 1439	21785 / 18 / 1454	21987 / 2 / 1404
GOF on F^2	1.040	1.081	1.070	1.004
R_1, wR_2 ($I>2\sigma(I)$)[a]	0.0452, 0.1046	0.0271, 0.0692	0.0405, 0.1086	0.0653, 0.1733
R_1, wR_2 (all data)	0.0602, 0.1099	0.0308, 0.0707	0.0465, 0.1117	0.0844, 0.1873

Table S2. The ratios of $I(^5D_0\rightarrow{}^7F_2)$ / $I(^5D_0\rightarrow{}^7F_1)$ for **4** in aqueous solution with different DPA concentrations.

C_{DPA}	$I(^5D_0\rightarrow{}^7F_2)$	$I(^5D_0\rightarrow{}^7F_1)$	ratio
0	63675.813	24022.391	2.651
25	64681.438	24961.701	2.591
50	67111.586	24579.338	2.730
75	69350.234	25729.549	2.695
100	72506.305	25175.031	2.880
125	75899.258	23641.924	3.210
150	78256.195	26268.303	2.979
175	80972.7813	26440.9141	3.062
200	84845.8203	25837.1758	3.284
225	86845.2422	27807.543	3.123
250	89668.6094	26691.5605	3.359
275	93189.4297	28469.9766	3.273
300	96212.6797	25850.9043	3.722
325	98736.7031	28384.6523	3.479
350	105197.3105	30837.5586	3.411

375	112554.1025	30378.7109	3.705
400	125073.1250	31405.9023	3.839

Table S3. The standard deviations for **4**-based FL sensor.

	I **(FL intensity of the peak at 614 nm)**	**AVG. (Average of *I*)**	**AVG. / *I***	**Standard deviation (*s*)**
Sample 1	58779.95		0.9969	
Sample 2	58551.65	58603.47	1.0009	2.681×10^{-3}
Sample 3	58478.82		1.0021	

The standard deviation ($s = 2.681 \times 10^{-3}$) calculated above and the slope k (0.0021) of the linear curve obtained are substituted into the equation LOD = 3s / k, and the detection limit is calculated as 3.83 μM.

Table S4. Performance comparison of several sensors for the detection of DPA.

Sensor	**Detection method**	**Linear**	**LOD**	**Real sample analysis**	**Ref.**
SiNPs-Eu^{3+}	Fluorometric	0.6-600 nM	0.2 nM		6
Pdots-Tb^{3+}	Fluorometric	0.2-64 nM	0.2 nM		7
DO2A-Tb^{3+}	Fluorometric	0-24 nM	6 nM	Bacterial endospores	8
g-C_3N_4/CitNa/Eu^{3+}	Fluorometric	0-15 μM	13 nM	tape water and orange juice	9
R6G/Eu-CdS@ZIF-8	Fluorometric	0.1-150 μM	67 nM	Bacterial endospores	10
GNPs-Tb^{3+} and Eu^{3+}	Fluorometric	0–100 μM	1 μM		11
BODIPY-Cu^{2+}	Colorimetric and fluorometric	0-10 μM	2 μM	Bacterial endospores	12
Eu-MOF	Fluorometric	0–100 μM	3.8 μM		13
R6H@Eu(BTC)	Colorimetric and fluorometric	0-120 μM / 0-80 μM	4.5 μM / 8.9 μM	water	14
Eu-POM	Fluorometric	0–325 μM	3.83 μM	Top water and Serum	this work

Table S5. Detection results of DPA in tap water and human serum sample.

Sample	**Found**	**Spiked (μM)**	**Measure (μM)**	**Recovery (%)**	**RSD (n = 3, %)**
Tap water	Not	30	28.49	94.98	1.66
		50	49.79	99.57	3.88
		70	69.88	99.83	1.20
Human serum	Not	30	31.30	104.35	6.80
		50	50.87	101.75	3.70
		70	67.68	96.68	6.37

Table S6. Summary of the lifetimes of $Eu(NO_3)_3 \cdot 6H_2O$ (3 mg / mL) in H_2O and D_2O with different DPA concentrations and the calculated q values.

CDPA / μM	T_{H2O} / ms	T_{D2O} / ms	q
0	0.112	2.702	9.0
100	0.114	2.831	8.9
200	0.115	2.893	8.8
300	0.116	2.976	8.7
400	0.117	2.995	8.7

References

[1] G. M. Sheldrick, SADABS: Program for Absorption Correction, University of Göttingen, Germany, **1997**.

[2] G. M. Sheldrick, SHELXS 97, Program for Crystal Structure Solution, University of Göttingen, Germany, **1997**.

[3] G. M. Sheldrick, SHELXL 97, Program for Crystal Structure Refinement, University of Göttingen, Germany, **1997**.

[4] H. L. Li, C. Lian, L. J. Chen, J. W. Zhao and G. Y. Yang, Two unusual nanosized Nd^{3+}-substituted selenotungstate aggregates simultaneously comprising lacunary Keggin and Dawson polyoxotungstate segments, *Nanoscale*, 2020, **12**, 16091–16101.

[5] (a) Y. J. Niu, Q. F. Xu, Y. Wang, Z. Li, J. K. Lu, P. T. Ma, C. Zhang, J. Y. Niu and J. P. Wang, Preparation, characterization, and catalytic performances of a pyrazine dicarboxylate-bridging rare-earth-containing polytungstoarsenate aggregate for selective oxidation of thiophenes and deep desulfurization of model fuels, *Dalton Trans*., 2018, **47**, 9677–9684.; (b) Q. Han, Z. Li, X. M. Liang, Y. Ding and S.-T. Zheng, Synthesis of a 6-nm-long transition-metal-rare-earth-containing polyoxometalate, *Inorg. Chem*., 2019, **58**, 12534–12537

[6] K. L. Ai, B. H. Zhang and L. H. Lu, Europium-based fluorescence nanoparticle sensor for rapid and ultrasensitive detection of an anthrax biomarker, *Angew. Chem. Int. Ed.*, 2009, **48**, 304–308.

[7] Q. Li, K. Sun, K. W. Chang, J. B. Yu, D. T. Chiu, C. F. Wu and W. P. Qin, Ratiometric luminescent detection of bacterial spores with terbium chelated semiconducting polymer Dots, *Anal. Chem*., 2013, **85**, 9087−9091.

[8] M. L. Cable, J. P. Kirby, K. Sorasaenee, H. B. Gray and A. Ponce, Bacterial spore detection by [Tb^{3+} (macrocycle)(dipicolinate)] Luminescence, *J. Am. Chem. Soc*., 2007, **129**, 1474–1475.

[9] M. Yuan, Y. Jin, L. Yu, Y. M. Bu, M. T. Sun, C. Yuan and S. H. Wang, Europium-modified carbon nitride nanosheets for smartphone-based fluorescence sensitive recognition of anthrax biomarker dipicolinic acid, *Food Chem*., 2023, **398**, 133884.

[10] X. Q. Li, J. J. Luo, L. Deng, F. H. Ma and M. H. Yang, In situ incorporation of fluorophores in zeolitic imidazolate framework-8 (ZIF-8) for ratio-dependent detecting a biomarker of anthrax spores, *Anal. Chem*., 2020, **92**, 7114−7122.

[11] M. Donmea, M. D. Yilmaz and B. Kilbas, Fluorescent detection of dipicolinic acid as a biomarker of bacterial spores using lanthanide-chelated gold nanoparticles, *J. Hazard. Mater*., 2017, **324**, 593−598.

[12] Y. Cetinkaya, M. N. Z. Yurt, H. A. Oktem and M. D. Yilmaz, A monostyryl boradiazaindacene (BODIPY)-based lanthanide-free colorimetric and fluorogenic probe for sequential sensing of copper (II) ions and dipicolinic acid as a biomarker of bacterial endospores, *J. Hazard. Mater*., 2019, **377**, 299−304.

[13] D. Wu, Z. Zhang, X. W. Chen, L. K. Meng, C. G. Li, G. H. Li, X. B. Chen, Z. Shi and S. H. Feng, A non-luminescent Eu-MOF-based ‘‘turn-on’’ sensor towards an anthrax biomarker through single-crystal to single-crystal phase transition, *Chem. Commun*., 2019, **55**, 14918−14921.

[14] K. Y. Shi, Z. C. Yang, L. H. Dong and B. Yu, Dual channel detection for anthrax biomarker dipicolinic acid: the combination of an emission turn on probe and luminescent metal-organic frameworks, *Sens. Actuators B Chem*., 2018, **266**, 263−269.